Archival Report

Biological Psychiatry: CNNI

# Awake Mouse Imaging: From Two-Photon Microscopy to Blood Oxygen Level–Dependent Functional Magnetic Resonance Imaging

Michèle Desjardins, Kıvılcım Kılıç, Martin Thunemann, Celine Mateo, Dominic Holland, Christopher G.L. Ferri, Jonathan A. Cremonesi, Baoqiang Li, Qun Cheng, Kimberly L. Weldy, Payam A. Saisan, David Kleinfeld, Takaki Komiyama, Thomas T. Liu, Robert Bussell, Eric C. Wong, Miriam Scadeng, Andrew K. Dunn, David A. Boas, Sava Sakadžić, Joseph B. Mandeville, Richard B. Buxton, Anders M. Dale, and Anna Devor

## ABSTRACT

**BACKGROUND:** Functional magnetic resonance imaging (fMRI) in awake behaving mice is well positioned to bridge the detailed cellular-level view of brain activity, which has become available owing to recent advances in microscopic optical imaging and genetics, to the macroscopic scale of human noninvasive observables. However, though microscopic (e.g., two-photon imaging) studies in behaving mice have become a reality in many laboratories, awake mouse fMRI remains a challenge. Owing to variability in behavior among animals, performing all types of measurements within the same subject is highly desirable and can lead to higher scientific rigor.

**METHODS:** We demonstrated blood oxygenation level–dependent fMRI in awake mice implanted with long-term cranial windows that allowed optical access for microscopic imaging modalities and optogenetic stimulation. We started with two-photon imaging of single-vessel diameter changes ($n$ = 1). Next, we implemented intrinsic optical imaging of blood oxygenation and flow combined with laser speckle imaging of blood flow obtaining a mesoscopic picture of the hemodynamic response ($n$ = 16). Then we obtained corresponding blood oxygenation level–dependent fMRI data ($n$ = 5). All measurements could be performed in the same mice in response to identical sensory and optogenetic stimuli.

**RESULTS:** The cranial window did not deteriorate the quality of fMRI and allowed alternation between imaging modalities in each subject.

**CONCLUSIONS:** This report provides a proof of feasibility for multiscale imaging approaches in awake mice. In the future, this protocol could be extended to include complex cognitive behaviors translatable to humans, such as sensory discrimination or attention.

*Keywords:* Blood oxygen level–dependent (BOLD) signal, Cerebral blood flow, fMRI, Intrinsic optical signals, Optogenetic, Two-photon microscopy

https://doi.org/10.1016/j.bpsc.2018.12.002

Noninvasive imaging technologies, such as functional magnetic resonance imaging (fMRI), positron emission tomography, and electroencephalography/magnetoencephalography, are widely used to investigate the function of the human brain. However, interpretation of these macroscopic signals in terms of the underlying microscopic physiology, such as electrical activity of single neurons and hemodynamic activity of single blood vessels, is still under investigation (1). Noninvasive imaging in experimental animals can play a critical role in physiological underpinning and data-driven modeling of human noninvasive signals, in particular when both microscopic and macroscopic measurements are achieved in the same subject under analogous experimental conditions.

The idea is to use state-of-the-art microscopic measurement technologies in the mouse to precisely and quantitatively probe concrete microscopic physiological parameters underlying macroscopic cerebral blood flow, oxygen consumption, and electrophysiological electroencephalography/magnetoencephalography signals, while manipulating cell type–specific neuronal activity (1). These measurements, which are available only in animals, provide the data needed for building computational bridges across spatial scales and imaging and recording modalities. For example, these microscopic measurements can be used to simulate the blood oxygenation level–dependent (BOLD) fMRI signal bottom-up (2–5). The end point result can then be validated against the actual mouse fMRI data (2). These simulations also provide the microscopic ground truth for the development and calibration of top-down macroscopic analytical fMRI models applicable to humans (6).

VIDEO CONTENT AVAILABLE WITH THIS ARTICLE



ISSN: 2451-9022

Our previous studies relied on fMRI data from anesthetized rodents. However, anesthesia can differentially affect neuronal cell types as well as blood flow and oxygen metabolism, altering neuronal network activity and neurovascular and metabolic coupling. To this end, the current report provides a protocol and a proof of feasibility for BOLD fMRI in awake mice implanted with long-term glass cranial windows that do not significantly deteriorate the quality of fMRI. These windows provide optical access for microscopic and mesoscopic optical imaging modalities and neuronal stimulation with light [also known as optogenetics (7)]. Therefore, alternating between the imaging modalities for each subject is possible.

Mice have become the species of choice for detailed, microscopic in vivo imaging studies of the mammalian brain. This is in part due to recent advances in transgenic technology that allow genetically targeted observation and manipulation of specific neuronal cell types. Novel genetically encoded probes of brain activity (e.g., genetically encoded calcium indicators) as well as tools for optogenetic (OG) neuronal excitation and inhibition have enabled new experimental paradigms in which awake mice undergo repeated microscopic imaging for the duration of weeks and months while performing behavioral tasks (8). These long-term imaging studies are free from confounds of anesthesia and have a higher potential for human translation.

Whereas optical imaging studies in awake behaving mice have become routine, their fMRI counterpart remains a challenge. Prior studies have leveraged the power of noninvasive fMRI in intact conscious rodents to map the brain response to drug administration (9) and sensory stimuli, including tactile (10) and nociceptive somatic (11) inputs as well as odorants (12) and conditioned visual stimuli (13). Following the first demonstration of feasibility for combining fMRI with optogenetics by Lee *et al.* (14), the repertoire of stimuli applicable to awake rodent fMRI has been extended to include OG excitation or inhibition (15–19). In these studies, the OG light stimulus was delivered via an optical fiber implanted into the brain. In the present study, we employed a long-term cranial window that allows OG stimulation as well as single-photon and multiphoton optical imaging of the cortical area within the window, enabling multiscale and multimodal imaging for each experimental subject. First, we describe installation and stability of our MRI-compatible headpost assembly including the cranial window. Then we provide illustrative data using optical imaging and fMRI in response to OG and sensory stimuli. In the present study, we used a simple air puff sensory stimulus. In the future, this protocol can be extended to include more complex cognitive behaviors translatable to humans, such as sensory discrimination or attention.

## METHODS AND MATERIALS

Some of the procedures were similar to procedures described in our previous study (20). For brevity, only novel aspects are described here. Detailed methods can be found in Supplemental Methods.

### Animal Procedures

The surgical procedure was modified from the procedure previously described by Goldey *et al.* (21) from Andermann's laboratory (see Supplemental Methods for details). The left barrel cortex was exposed over a 3-mm-diameter circular area with the center coordinates of anterior-posterior 2 mm and left-right 3 mm (relative to bregma) and sealed with the glass window implant (Figure 1A). A plastic headpost, used for immobilization of the head during imaging, was glued to the bone contralateral to the glass implant (Figure 1B). To standardize the position of the imaging window across subjects, the headpost was lowered onto the bone while mounted onto a stereotactic manipulator ensuring a fixed angle and orientation.

### Imaging

Following behavioral training, the animals were imaged using two-photon microscopy for single-vessel diameter measurements, spectral and laser speckle (LS) contrast imaging to measure blood oxygenation and flow, and BOLD fMRI. The BOLD fMRI methods are presented below; other methods can be found in Supplemental Methods.

### Blood Oxygen Level–Dependent fMRI

Magnetic resonance images were acquired on a 7T/11-cm horizontal bore scanner (BioSpec 70/20 USR; Bruker Corp., Billerica, MA). The 7T scanner was equipped with a BGA 12S2 gradient set with 440 mT/m gradient strength and 3440 T/m/s slew rate. A custom-made 2 × 3 cm-diameter surface radiofrequency coil was used to transmit and receive the radiofrequency signal. BOLD fMRI data were acquired using a single-shot gradient-echo echo-planar imaging (EPI) pulse sequence with the following parameters: echo time = 11–20 ms, repetition time = 1 second, flip angle = 45°, matrix = 100 (read, left/right) × 50 (phase encoding, superior/inferior) over a 2 × 1 cm field of view, slice thickness = 1 mm, five adjacent coronal slices in interleaved order. High-resolution rapid acquisition with relaxation enhancement (TurboRARE) structural images were obtained of the same slices to identify brain structures and the location of the optical window (Supplemental Figure S5). TurboRARE images had the same slice thickness as EPI images but higher in-plane resolution (256 × 128 for TurboRARE vs. 100 × 50 for EPI).

Mice were briefly (<60 seconds) anesthetized during head fixation in a custom-made MRI-compatible mouse cradle (Supplemental Figure S1C) and insertion of ear plugs (cut from commercial human-size silicon ear plugs). Once in the bore, coil stability was ensured by inflating three pneumatic air chambers of the cradle to absorb vibrations. After manual coil matching and tuning, images were acquired in the following order: an anatomical localizer (TurboRARE), gradient-echo EPI functional scans, spin echo in forward and reverse directions for distortion correction (see below).

Motion correction was implemented by aligning each EPI image in a time series to the first one using in-house written rigid body registration software based on MATLAB imregister function (The MathWorks, Inc., Natick, MA). Correction of image distortion owing to $B_0$ field inhomogeneity induced by magnetic susceptibility variations was implemented using our previously published method, which involves acquisition of two spin-echo images with opposite phase encoding directions (22). EPI images were spatially smoothed with a 3-pixel full width at half maximum Gaussian kernel. Ratio

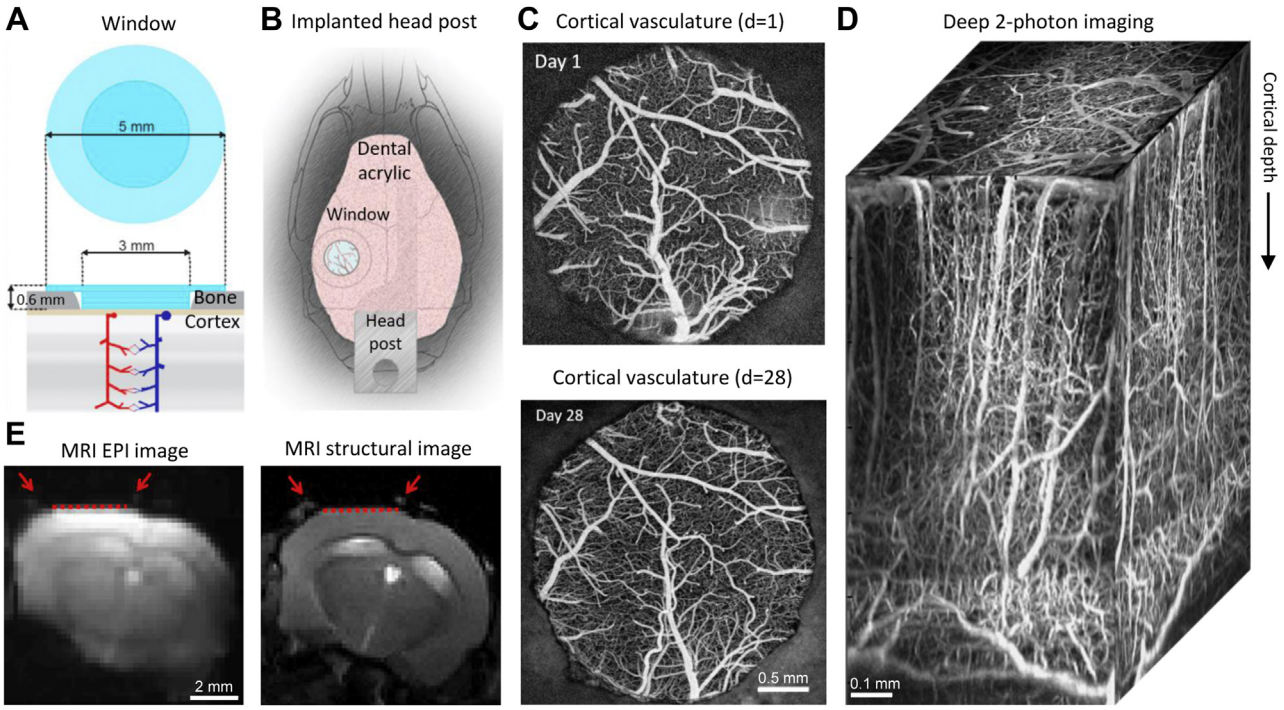


**Figure 1.** Magnetic resonance imaging (MRI)–compatible headpost assembly and image quality across modalities. **(A)** Schematics of the borosilicate glass window implant. **(B)** Schematic illustration of the window implant over the whisker representation within the primary somatosensory cortex and the headpost fixed to the skull overlaying the other (contralateral) hemisphere. **(C)** Images of the brain vasculature through the glass window implant obtained by two-photon imaging of fluorescein isothiocyanate–labeled dextran injected intravenously. The images illustrate preserved integrity of the vasculature between days 1 (top panel) and 28 (bottom panel) following surgical implantation. **(D)** Two-photon image stack obtained with Alexa 680–labeled dextran injected intravenously illustrating the capability of deep imaging. **(E)** Corrected gradient-echo echo-planar image (EPI) (left panel) and corresponding structural image (high-resolution rapid acquisition with relaxation enhancement) (right panel). Red arrows point to the peripheral edges of the implant, i.e., the glass/bone boundary. Red dotted line indicates the bottom of the glass implant, i.e., the glass/brain boundary.

images were defined relative to a prestimulus baseline (2 seconds for event-related design, 5 seconds for blocked design) and averaged over stimulus trials. Realigned, smoothed images were entered into a general linear model using SPM12 (Wellcome Trust Centre for Neuroimaging, London, United Kingdom) and a canonical hemodynamic response function with time derivatives. Using a finite impulse response model yielded very similar results (not shown). A *t* statistic contrast was used to identify voxels where the signal significantly differed from baseline, i.e., activated voxels. The statistical map was thresholded at $p = .001$ uncorrected to define a region of interest for time-course extraction.

### Stimulus Paradigm

For sensory stimulation, each trial consisted of a 2-second train of air puffs at 3 Hz delivered to the lower bottom part of the contralateral whisker pad to avoid an eye blink; we used 10 trials per run with 20-second interstimulus interval. For the blocked stimulus, the puffs were delivered at 5 Hz for 20 seconds. During OG stimulation, each trial consisted of a train of 5-ms blue light pulses delivered at 100 Hz during 100 ms (equivalent to a single 100-ms pulse at 50% duty-cycle); we used 10 trials per run with 20-second interstimulus interval. For the blocked stimulus, the 100-ms trains were repeated at 1 Hz for 20 seconds with eight trials per run. In fMRI and intrinsic optical imaging/speckle contrast imaging, the OG light was delivered to the surface of the window by means of an optical fiber placed approximately 0.5 mm above the glass window creating an approximately 1 mm circular illumination spot. In two-photon experiments, the OG light was delivered through the objective (20). Laser power was 6 to 8 mW under the objective (for two-photon imaging) or at the fiber tip (for optical intrinsic signals [OIS] and LS imaging). In the control experiments in wild-type mice, laser power at the tip of the fiber was 12 mW.

## RESULTS

The goal for this study was to establish a protocol for long-term imaging of awake behaving mice using different measurement modalities, including two-photon imaging and fMRI, in each subject. Our criteria for success were as follows: 1) sufficient optical clarity of the window to allow two-photon imaging throughout the cortical depth as well as single-photon imaging, 2) minimal loss of the BOLD fMRI signal owing to unwanted susceptibility artifacts, 3) sufficient mechanical stability of the MRI-compatible headpost assembly to allow state-of-the-art two-photon imaging under analogous head fixation to that used in fMRI experiments, 4) stability over time for longitudinal imaging for durations of weeks and months, and 5) compatibility with behavioral experiments. We

describe our design below and illustrate the imaging capabilities.

## MRI-Compatible Headpost Assembly

We used glass window implants previously described by Goldey *et al*. (21). The implant was prepared ahead of time and consisted of three 3-mm round coverslips and a single 5-mm coverslip, all made of borosilicate glass (#1 thickness, CS-3R and CS-5R; Warner Instruments LLC, Hamden, CT) and glued together using optical adhesive (Norland Optical Adhesive 61; Norland Products, Inc., Cranbury, NJ) that was cured with ultraviolet light (SpotCure-B6; Kinetic Instruments Inc., Bethel, CT) (Figure 1A). The headpost, needed for immobilization of the mouse head during imaging, was custom machined from polyether ether ketone, an MRI-compatible hard plastic material (Figure 1B). Premade glass window implants and polyether ether ketone headposts were kept in 70% ethanol until implantation.

Borosilicate glass differs from the brain tissue (mostly composed of water) in its magnetic susceptibility index (23). For two-dimensional pulse sequences using relatively thick slices (in our case, 1 mm), this mismatch can lead to a susceptibility signal loss owing to within-voxel, through-plane variation of the $B_0$ field. Therefore, we standardized the position of the imaging window to ensure alignment of the glass/brain interface with the $B_0$ vector of the MRI scanner. To this end, the window and the headpost were fixed to the skull in a predetermined orientation such that when the mouse head was immobilized in the MRI cradle, the normal angle to the window plane would be orthogonal to $B_0$ (see Methods and Materials). In this way, susceptibility artifacts owing to the window were limited to the perimeter of the implant.

In agreement with previous studies that used this type of cranial implant for two-photon imaging (21), the window remained clear and transparent for durations of weeks and months (Figure 1C) allowing imaging throughout the cortical depth and down to the white matter (Figure 1D). The quality of BOLD fMRI images depended to a large extent on the quality of the surgical preparation. Even after weeks of healing, residues of dry blood on the skull around the implant created signal loss and image distortion owing to $B_0$ field inhomogeneity induced by magnetic susceptibility variations. Image distortion was corrected using our previously published method that involves acquisition of spin-echo EPI scans with opposite phase encoding polarities (22). Reversing the phase-encoding direction resulted in opposite spatial distortion patterns. These data were then used to recover the correct image geometry of the target gradient-echo EPI scan (Figure 1E and Supplemental Figure S1A, B).

In all cases, BOLD fMRI images experienced some degree of signal loss at the edge of the borosilicate glass implant (red arrows in Figure 1E). This artifact, however, was well localized to the perimeter of the window and did not significantly affect the quality of the BOLD signal immediately under the implant.

## Compatibility With Optical Imaging Across Scales

Cranial glass windows allow optical imaging across scales that can be very informative for physiological underpinning of fMRI signals (20,24,25), particularly when the fMRI study is conducted in the same animal subject. On the microscopic scale, neuronal, glial, vascular, and metabolic activity can be measured with submicron resolution using two-photon imaging. Figure 2A–C illustrates an example of time-resolved imaging of single-vessel dilation, which is a key parameter in detailed models of fMRI signals (2,6). These data were obtained by an intravascular injection of a fluorescent contrast agent (fluorescein isothiocyanate or Alexa Fluor 680 conjugated to dextran; see Supplemental Methods) and tracking the vessel diameter as a function of time. In this example, we used a VGAT-ChR2(H134R)-EYFP mouse in which all inhibitory interneurons expressed the OG actuator channelrhodopsin-2 (26). The OG stimulus consisted of a single 100-ms pulse of blue light (473 nm) delivered through the objective (20). In addition, we used a sensory stimulus, which consisted of three air puffs delivered at 3 Hz to the whisker pad contralateral to the imaging window. If desired, two-photon imaging can be used to extract other parameters, including measures of neuroglial activity (24,27–29), intravascular or tissue oxygenation (30–34), oxygen consumption (35), and glucose metabolism (36). Figure 2D–E and Supplemental Figure S2A show the corresponding mesoscopic changes in blood oxygenation and flow obtained in the same subject under the same stimulus conditions using single-photon charge-coupled device–based imaging. In this example, we used simultaneous hemoglobin-based OIS imaging and LS contrast imaging (37–39) to obtain changes in oxyhemoglobin, deoxyhemoglobin, and blood flow in response to OG and sensory stimulation. The OG stimulus was delivered via an optical fiber positioned approximately 0.5 mm above the window at an angle of approximately 60° to avoid reflection from the glass surface (Figure 2D) using the same stimulus parameters as for two-photon imaging shown in Figure 2C. Presenting the same OG stimulus in wild-type animals did not cause significant oxyhemoglobin and deoxyhemoglobin changes (Supplemental Figure S2B), arguing against potential effects of heat generated by the 473-nm laser within our range of laser power (40,41). The sensory stimulus was the same as for two-photon measurements (Figure 2C). For two-photon imaging, we rejected stimulus trials with large motion artifacts that could be identified by analysis of the surveillance video (see Methods and Materials) and/or unrealistically large signal changes. Sensory stimuli generated motion more often compared with OG stimuli: approximately 15% to 20% of trials were rejected for sensory stimuli, and approximately 5% to 10% were rejected for OG stimuli. OIS imaging is more robust against motion artifacts, and thus no trials were rejected. Some studies used sedation to mitigate motion artifacts (27). In our study, however, sedation with 1 to 2 mg/kg chlorprothixene (Sigma-Aldrich, St. Louis, MO) notably slowed down the hemodynamic response kinetics (Supplemental Figure S2C). Thus, sedation is not recommended as a means of providing image stability in quantitative hemodynamic and neurovascular coupling studies.

## BOLD fMRI in Mice With Long-term Cranial Windows

Mesoscopic OIS and LS contrast measures can serve as a proxy for the BOLD fMRI signal (42–45). However, the measurement theory for each of these measurement technologies

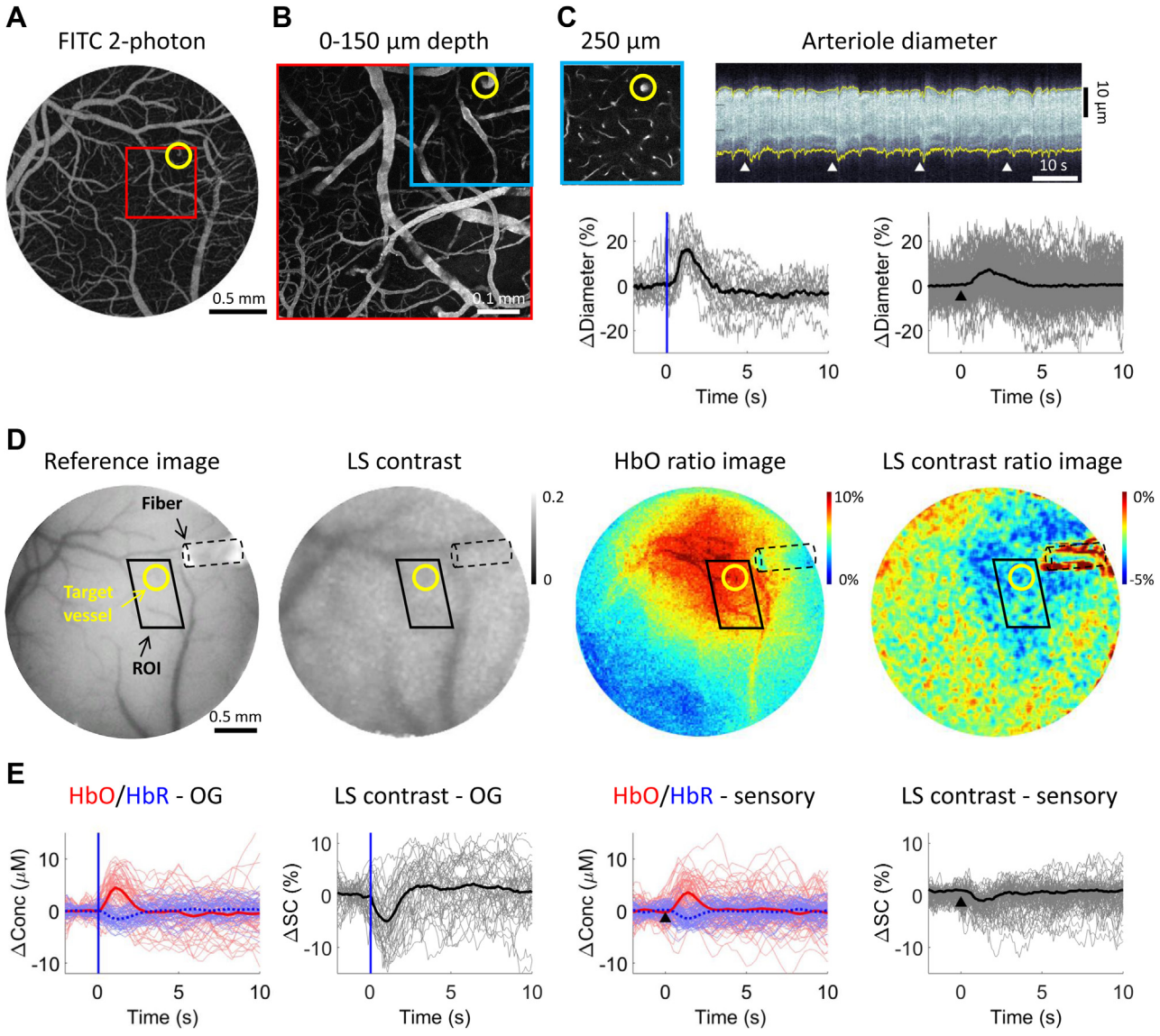


**Figure 2.** From two-photon microscopy to mesoscopic optical intrinsic signals/laser speckle (LS) imaging providing a proxy for the blood oxygen level–dependent signal. **(A)** Image of the surface vasculature calculated as a maximal intensity projection of an image stack 0–300 µm in depth using a 4× objective. Individual images were acquired every 10 µm. **(B)** Zoomed-in view of the region within the red square in panel **(A)** acquired with a 20× objective. **(C)** (Top left panel) Plane 250 µm below the surface corresponding to the region outlined in blue in panel **(B)**. Yellow circle indicates a small diving arteriole. (Top right panel) Example temporal diameter change profile acquired from the arteriole outlined by the yellow circle imaged 250 µm below the surface. The vessel diameter was captured by repeated line scans across the vessel. These line scans form a space-time image when stacked sequentially from left to right. White arrowheads indicate the onset of stimulus trials (air puffs to the whisker pad); four trials are shown. (Bottom panel) Single-vessel dilation time courses extracted from data such as that illustrated in panel **(C)**. Time courses for individual trials are overlaid for optogenetic (OG) stimulus (left graph; $n$ = 19 trials) and sensory stimulus (right graph; $n$ = 160 trials); the thick lines show the average. The stimulus onset is indicated by a blue vertical line and black arrowhead for the OG and sensory panels, respectively. **(D)** Concurrent optical intrinsic signals and LS contrast imaging in the same subject as in panels **(A–C)**. (Left panel) Charge-coupled device reflectance image of the surface vasculature. (Middle panel) The corresponding LS contrast image. (Right panel) Ratio images of oxyhemoglobin (HbO) (extracted from the optical intrinsic signals data; see Methods and Materials) and LS contrast showing the region of activation following OG stimulation. The location of optical fiber is indicated on all images (black dotted line). The same arteriole as in panel **(C)** is outlined by yellow circles. The black parallelogram indicates the region of interest (ROI) used for extraction of time courses in panel **(E)**. **(E)** Time-courses of HbO and deoxyhemoglobin (HbR) (shown in red and blue, respectively) and LS contrast (shown in black) in response to OG and sensory stimulation. These time courses were extracted from the polygonal ROI shown in panel **(D)**. Conc, concentration; FITC, fluorescein isothiocyanate; SC, speckle contrast.

is unique, relying on different assumptions across different imaging methods (46). Therefore, direct acquisition of the fMRI data is highly desirable to ensure consistency of the modeling/integration framework (1,2). To this end, we performed BOLD fMRI in mice with long-term cranial windows in response to OG and sensory stimulation. OG stimulus was delivered via an optical fiber similar to that used in the OIS and LS imaging experiments. The fiber was positioned in the middle of the

radiofrequency coil ending approximately 0.5 mm above the glass window at an angle of approximately 70° (see Methods and Materials and Supplemental Figure S1C). As we used a small surface radiofrequency coil to transmit and receive (see Methods and Materials), our sensitivity decreased with distance from the coil, resulting in an inhomogeneous signal-to-noise ratio within the image. Therefore, we thresholded EPI images at approximately 40% of the maximum intensity to limit our analysis to pixels with high signal-to-noise ratio. Figure 3 illustrates BOLD fMRI responses to a 20-second train of 100-ms light pulses delivered at 1 Hz (Figure 3A–C, analogous to a blocked design) and a single 100-ms light pulse (Figure 3D and E, analogous to an event-related design) from a single fully awake Emx1-Cre;Ai32 subject where channelrhodopsin-2 was expressed in pyramidal cells (47,48). BOLD ratio images (Figure 3A, D) were calculated relative to the prestimulus baseline using a single slice cutting through the center of the evoked response. This presentation facilitates the comparison with OIS imaging if needed (25). The BOLD signal change in response to both stimulus conditions localized to the cortical tissue within the cranial window. The same data can also be viewed as *p* value maps; statistically significant activation localized to the cortical area within the window was detected for the blocked design (Figure 3C). Time courses extracted from the active region of interest, which was defined by thresholding of the *p* value map, revealed a high degree of temporal signal fluctuation (Figure 3B, E and Supplemental Figure S3), most likely owing to spontaneous neuronal activity (49,50) as well as residual movement artifacts. On average, an increase in the BOLD signal was visible for both stimulus conditions (thick lines in Figure 3B, E and Supplemental Figure S3). Comparison of the BOLD response time course with that obtained by OIS and LS imaging revealed a consistent shape across the measurement modalities for the same stimulus condition (Supplemental Figure S4).

Sensory stimulus in fMRI experiments consisted of air puffs delivered at 3 to 5 Hz to the whisker pad contralateral to the cranial window for a total duration of 20 seconds (blocked design) or 2 seconds (event-related design). Figure 4 shows an illustrative BOLD response in a fully awake mouse. As for the OG stimulus, BOLD signal change in response to both stimulus conditions localized to the cortical region within the window (Figure 4A, D), and an increase in the BOLD signal was visible for both stimulus conditions in trial-averaged time courses (Figure 4B, E). Statistically significant activation was detected for the blocked design (Figure 4C). As with two-photon imaging, we rejected stimulus trials with significant motion identified by analysis of the surveillance video (see Methods and Materials and Supplemental Video). When significant motion occurred somewhere within a stimulus trial, we always rejected

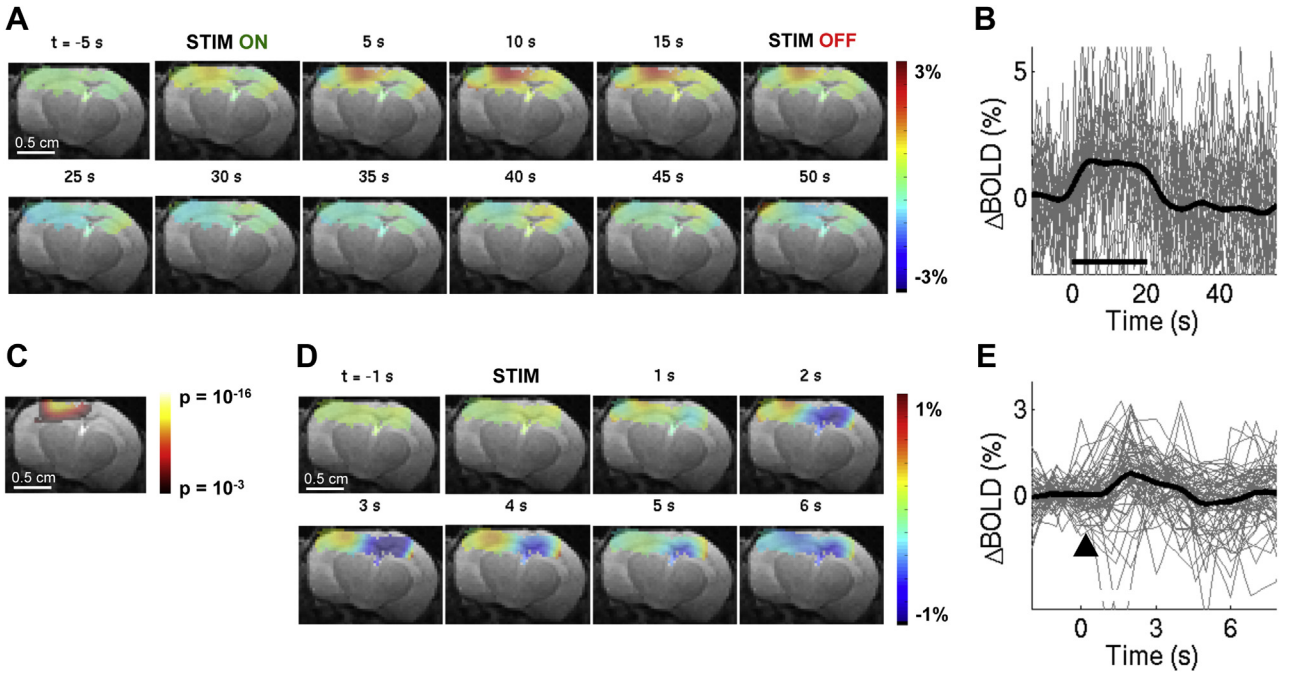


**Figure 3.** The blood oxygen level–dependent (BOLD) signal in response to optogenetic stimuli in a fully awake mouse. **(A)** Spatiotemporal evolution of BOLD signal change from a single slice cutting through the center of the evoked response, presented as trial-averaged ratio maps, in response to a 20-second train of 100-ms light pulses delivered at 1 Hz (blocked optogenetic stimulus) in a single Emx1-Cre;Ai32 subject. Echo-planar images were thresholded to reflect the sensitivity of the surface radiofrequency coil (for display purposes only). The ratio images are overlaid on the structural (high-resolution rapid acquisition with relaxation enhancement) image of the same slice. **(B)** BOLD response time courses extracted from the active region of interest. Twenty-eight stimulus trials are superimposed. The average is overlaid in thick black. For the full range of the y-axis, see Supplemental Figure S3. **(C)** Thresholded ($p$ = .001 uncorrected) statistical $p$ map corresponding to the data shown in panel **(A)** assuming the standard hemodynamic response function with temporal derivatives (see Methods and Materials). This map was used to define the region of interest for extraction of time courses in panels **(B)** and **(E)**. **(D)** As in panel **(A)** for single 100-ms light pulses (event-related optogenetic stimulus) in the same subject. **(E)** BOLD response time courses corresponding to panel **(D)**. Sixty-nine stimulus trials are superimposed. The average is overlaid in thick black. STIM, stimulus.

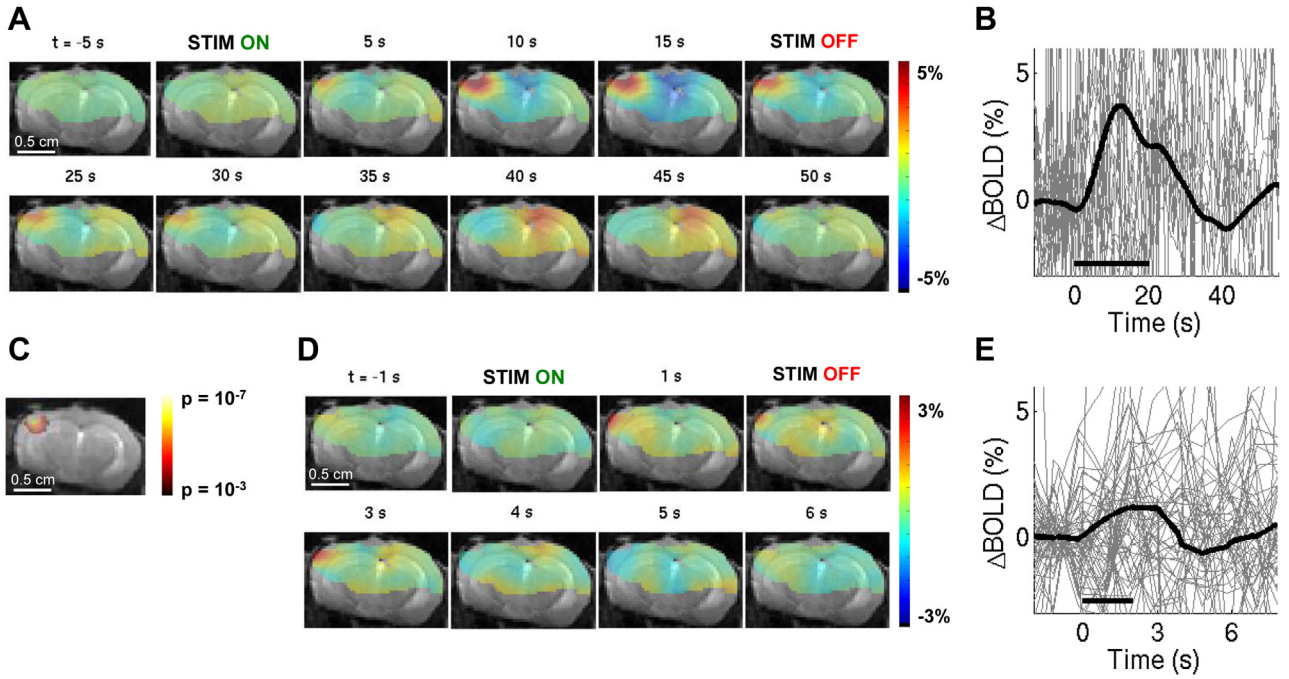


**Figure 4.** The blood oxygen level–dependent (BOLD) signal in response to sensory stimuli in a fully awake mouse. Conventions are the same as in Figure 3. Panels **(A–C)** correspond to 20-second stimulus duration ($n$ = 21 trials). Panels **(D–E)** correspond to 2-second stimulus duration ($n$ = 57 trials). For the full range of the y-axis for BOLD signal time courses, see Supplemental Figure S3. STIM, stimulus.

the entire trial. The proportion of rejected trials was similar to that in two-photon imaging: approximately 15% to 20% and approximately 5% to 10% for sensory and OG stimuli, respectively.

In contrast to Figures 3 and 4, where the mouse was fully awake, Figure 5 shows fMRI data acquired under sedation with chlorprothixene. In this case, we observed a larger spread of OG-induced activity, including the contralateral hemisphere (Figure 5A). The highest BOLD response, however, was well mapped to the cortical tissue under the window (Figure 5B). Sedated animals had lower baseline signal fluctuations, probably explained by reduced neuronal activity and body movement (Figure 5C, D and Supplemental Figure S3). Thus, while not appropriate for quantitative hemodynamic studies (Supplemental Figure S2C), BOLD fMRI in sedated mice may still be useful for troubleshooting the protocol and procedure. This is due to high signal-to-noise ratio of the BOLD signal and limited motion artifacts in sedated animals. Also, no trials were rejected owing to motion under sedation.

## DISCUSSION

In the present study, we have achieved BOLD fMRI in fully awake mice, implanted with long-term optical windows, in response to sensory and OG stimuli. Compared with our published data from rats anesthetized with α-chloralose (25), the BOLD signal induced by sensory stimulation in awake mice was approximately three times smaller when normalized by the corresponding averaged arteriolar dilation [awake mice in the present study: approximately 0.5% BOLD, approximately 7% dilation; anesthetized rats in study by Tian *et al.* (25): approximately 2% BOLD, approximately 10% dilation]. This difference can be caused by slower baseline blood flow under anesthesia leading to an increase in the fraction of oxygen extracted from blood by tissue. Hypothetically, if the baseline neuronal activity and cerebral metabolic rate of oxygen remain the same, slower flow would lead to a higher oxygen extraction fraction resulting in higher amount of deoxyhemoglobin in the voxel and lower baseline level of the BOLD signal. Thus, we speculate that if α-chloralose anesthesia affects the baseline blood flow more that it affects neuronal activity and neurovascular coupling, the stimulus may produce a greater ΔBOLD signal between the baseline and stimulated conditions. An alternative explanation for the low BOLD signal in response to sensory stimulation in the present study may be reduced attention of the animals to the stimulus during BOLD fMRI acquisition. Our animals were well trained and habituated to the noise of an EPI pulse sequence used for BOLD acquisition, head fixation, and light-emitting diode lighting as well as to wearing protective ear plugs (see Methods and Materials). However, we cannot rule out that some environmental factors, e.g., a residual vibration transmitted through the air cushions, distracted the animals' attention to the air puff.

In conclusion, the present study provides a proof-of-principle demonstration for using long-term optical cranial windows in animal BOLD fMRI studies. These windows support multimodal optical imaging, from detailed two-photon microscopy throughout the cortical depth and beyond to mesoscopic and macroscopic optical imaging using all available optical contrast mechanisms. We demonstrate that the presence of the window results in minimal losses of the BOLD

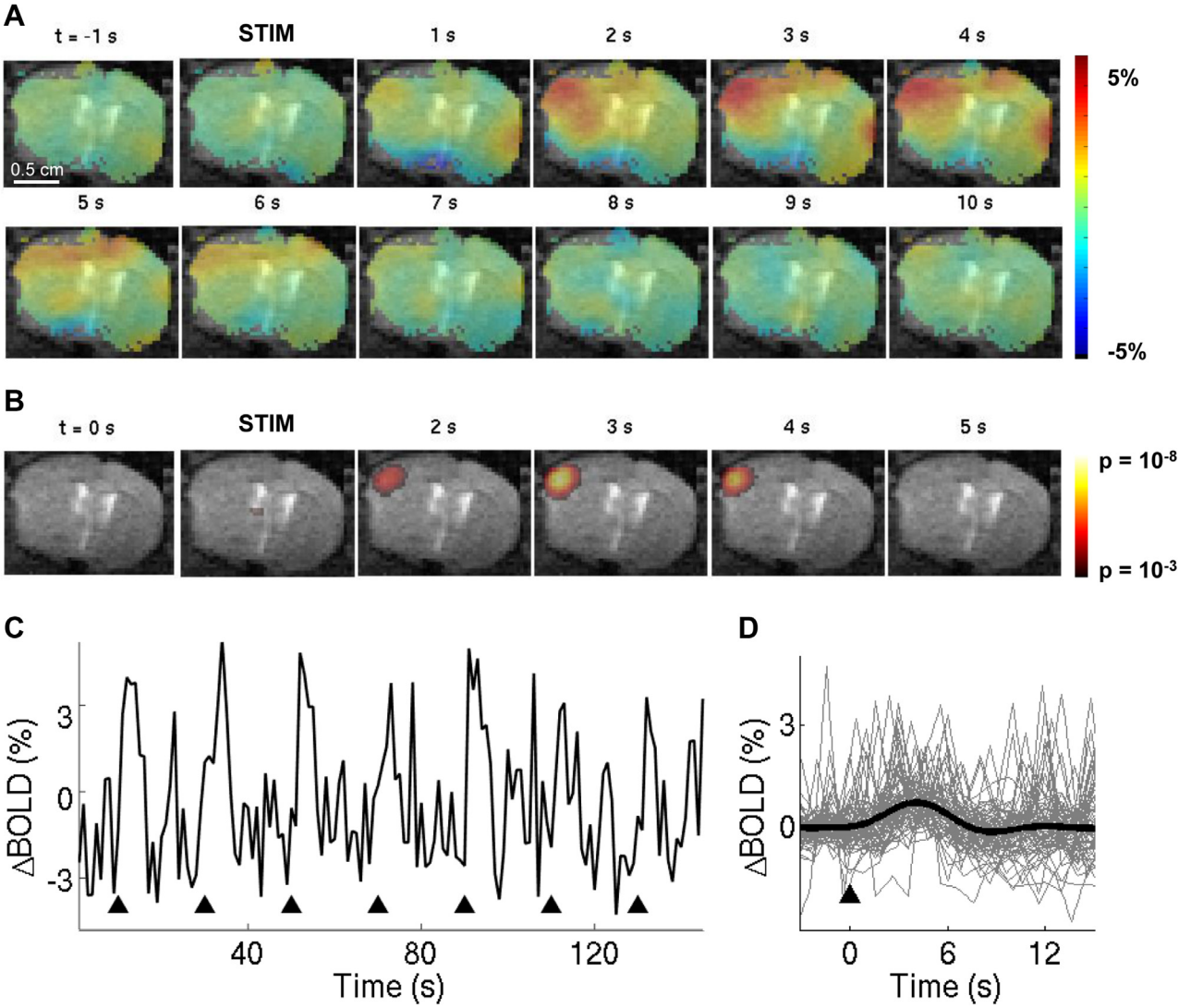


**Figure 5.** The blood oxygen level–dependent (BOLD) signal under sedation with chlorprothixene. **(A)** Spatiotemporal evolution of BOLD signal change from a single slice cutting through the center of the evoked response, presented as ratio maps, in response to single 100-ms light pulses in a sedated Emx1-Cre;Ai32 subject. **(B)** Corresponding time-resolved *p* maps. In this case, we made no assumptions about the shape of the hemodynamic response function (i.e., using a finite impulse response model). **(C)** BOLD signal time course from the active region of interest (defined by thresholding of the *p* value map). Black arrowheads indicate onset on stimulation trials. **(D)** Superimposed BOLD response time courses for 72 stimulus trials. The average is overlaid in thick black. STIM, stimulus.

fMRI signal, while allowing OG stimulation by simply positioning an optical fiber next to the window. These windows are stable and support longitudinal imaging alternating between imaging modalities for each subject over weeks and months. In the future, sampling multiple physiological parameters in an awake behaving mouse across scales and measurement modalities, including BOLD fMRI, will be instrumental for bridging BOLD fMRI signals induced by a complex behavior to the underlying activity of neuronal circuits. The ability to perform longitudinal studies while alternating between imaging modalities and manipulating neuronal activity with OG tools can also facilitate neurophysiological underpinning of spontaneous (resting-state) hemodynamic fluctuations (49–52) as well as cortical MRI signals in response to clinically relevant perturbations of brain activity (53).

## ACKNOWLEDGMENTS AND DISCLOSURES

This work was supported by the National Institutes of Health (Grant Nos. MH111359, NS057198, U01NS094232, and S10RR029050), Natural Sciences and Engineering Research Council of Canada (to MD), International Headache Society (to KK), Scientific and Technological Research Council of Turkey (to KK), and German Research Foundation (Grant No. DFG TH 2031/1 [to MT]).

The authors report no biomedical financial interests or potential conflicts of interest.

## ARTICLE INFORMATION

From the Department of Radiology (MD, TTL, RB, ECW, MS, RBB, AMD, AD), Department of Neurosciences (KK, MT, DH, CGLF, QC, KLW, PAS, TK, AMD, AD), Department of Physics (CM, DK), Biology Undergraduate Program (JAC), Section of Neurobiology (DK, TK), and Department of Electrical and Computer Engineering (DK), University of California, San Diego, La

Jolla, California; Martinos Center for Biomedical Imaging (BL, SS, JBM, AD), Massachusetts General Hospital, Harvard Medical School, Charlestown; Department of Biomedical Engineering (DAB), Boston University, Boston, Massachusetts; and Department of Biomedical Engineering (AKD), University of Texas at Austin, Austin, Texas.

MD is currently affiliated with Département de Physique, de Génie Physique et d'Optique, Université Laval and Centre de Recherche du Centre Hospitalier Universitaire de Québec–Université Laval, axe Oncologie, Québec, Canada.

KK is currently affiliated with Department of Biomedical Engineering, Boston University, Boston, Massachusetts.

MD and KK equally contributed to this work.

Address correspondence to Michèle Desjardins, Ph.D., Université Laval, Pavillon CHUL, 2705, Boulevard Laurier, Quebec, Quebec G1V 0A6, Canada; E-mail: michele.desjardins@phy.ulaval.ca.

Received Jul 12, 2018; revised Oct 26, 2018; accepted Nov 27, 2018.

Supplementary material cited in this article is available online at https://doi.org/10.1016/j.bpsc.2018.12.002.

## REFERENCES

1. Uhlirova H, Kilic K, Tian P, Sakadzic S, Gagnon L, Thunemann M, *et al.* (2016): The roadmap for estimation of cell-type-specific neuronal activity from non-invasive measurements. Philos Trans R Soc Lond B Biol Sci 371(1705).
2. Gagnon L, Sakadzic S, Lesage F, Musacchia JJ, Lefebvre J, Fang Q, *et al.* (2015): Quantifying the microvascular origin of BOLD-fMRI from first principles with two-photon microscopy and an oxygen-sensitive nanoprobe. J Neurosci 35:3663–3675.
3. Gagnon L, Smith AF, Boas DA, Devor A, Secomb TW, Sakadzic S (2016): Modeling of cerebral oxygen transport based on in vivo microscopic imaging of microvascular network structure, blood flow, and oxygenation. Front Comput Neurosci 10:82.
4. Fang Q, Sakadzic S, Ruvinskaya L, Devor A, Dale AM, Boas DA (2008): Oxygen advection and diffusion in a three-dimensional vascular anatomical network. Opt Express 16:17530–17541.
5. Boas DA, Jones SR, Devor A, Huppert TJ, Dale AM (2008): A vascular anatomical network model of the spatio-temporal response to brain activation. Neuroimage 40:1116–1129.
6. Gagnon L, Sakadzic S, Lesage F, Pouliot P, Dale AM, Devor A, *et al.* (2016): Validation and optimization of hypercapnic-calibrated fMRI from oxygen-sensitive two-photon microscopy. Philos Trans R Soc Lond B Biol Sci 371(1705).
7. Deisseroth K (2015): Optogenetics: 10 years of microbial opsins in neuroscience. Nat Neurosci 18:1213–1225.
8. Makino H, Komiyama T (2015): Learning enhances the relative impact of top-down processing in the visual cortex. Nat Neurosci 18:1116–1122.
9. Ferris CF, Yee JR, Kenkel WM, Dumais KM, Moore K, Veenema AH, *et al.* (2015): Distinct BOLD activation profiles following central and peripheral oxytocin administration in awake rats. Front Behav Neurosci 9:245.
10. Chang PC, Procissi D, Bao Q, Centeno MV, Baria A, Apkarian AV (2016): Novel method for functional brain imaging in awake minimally restrained rats. J Neurophysiol 116:61–80.
11. Yee JR, Kenkel W, Caccaviello JC, Gamber K, Simmons P, Nedelman M, *et al.* (2015): Identifying the integrated neural networks involved in capsaicin-induced pain using fMRI in awake TRPV1 knockout and wild-type rats. Front Syst Neurosci 9:15.
12. Ferris CF, Kulkarni P, Toddes S, Yee J, Kenkel W, Nedelman M (2014): Studies on the Q175 knock-in model of Huntington's disease using functional imaging in awake mice: Evidence of olfactory dysfunction. Front Neurol 5:94.
13. Harris AP, Lennen RJ, Marshall I, Jansen MA, Pernet CR, Brydges NM, *et al.* (2015): Imaging learned fear circuitry in awake mice using fMRI. Eur J Neurosci 42:2125–2134.
14. Lee JH, Durand R, Gradinaru V, Zhang F, Goshen I, Kim DS, *et al.* (2010): Global and local fMRI signals driven by neurons defined optogenetically by type and wiring. Nature 465:788–792.
15. Kolodziej A, Lippert M, Angenstein F, Neubert J, Pethe A, Grosser OS, *et al.* (2014): SPECT-imaging of activity-dependent changes in regional cerebral blood flow induced by electrical and optogenetic self-stimulation in mice. Neuroimage 103:171–180.
16. Liang Z, Watson GD, Alloway KD, Lee G, Neuberger T, Zhang N (2015): Mapping the functional network of medial prefrontal cortex by combining optogenetics and fMRI in awake rats. Neuroimage 117:114–123.
17. Aksenov DP, Li L, Miller MJ, Wyrwicz AM (2016): Blood oxygenation level dependent signal and neuronal adaptation to optogenetic and sensory stimulation in somatosensory cortex in awake animals. Eur J Neurosci 44:2722–2729.
18. Brocka M, Helbing C, Vincenz D, Scherf T, Montag D, Goldschmidt J, *et al.* (2018): Contributions of dopaminergic and non-dopaminergic neurons to VTA-stimulation induced neurovascular responses in brain reward circuits. Neuroimage 177:88–97.
19. Desai M, Kahn I, Knoblich U, Bernstein J, Atallah H, Yang A, *et al.* (2011): Mapping brain networks in awake mice using combined optical neural control and fMRI. J Neurophysiol 105:1393–1405.
20. Uhlirova H, Kilic K, Tian P, Thunemann M, Desjardins M, Saisan PA, *et al.* (2016): Cell type specificity of neurovascular coupling in cerebral cortex. Elife 5.
21. Goldey GJ, Roumis DK, Glickfeld LL, Kerlin AM, Reid RC, Bonin V, *et al.* (2014): Removable cranial windows for long-term imaging in awake mice. Nat Protoc 9:2515–2538.
22. Holland D, Kuperman JM, Dale AM (2010): Efficient correction of inhomogeneous static magnetic field-induced distortion in echo planar imaging. Neuroimage 50:175–183.
23. Wapler MC, Leupold J, Dragonu I, von Elverfeld D, Zaitsev M, Wallrabe U (2014): Magnetic properties of materials for MR engineering, micro-MR and beyond. J Magn Reson 242:233–242.
24. Nizar K, Uhlirova H, Tian P, Saisan PA, Cheng Q, Reznichenko L, *et al.* (2013): In vivo stimulus-induced vasodilation occurs without IP3 receptor activation and may precede astrocytic calcium increase. J Neurosci 33:8411–8422.
25. Tian P, Teng IC, May LD, Kurz R, Lu K, Scadeng M, *et al.* (2010): Cortical depth-specific microvascular dilation underlies laminar differences in blood oxygenation level-dependent functional MRI signal. Proc Natl Acad Sci U S A 107:15246–15251.
26. Zhao S, Ting JT, Atallah HE, Qiu L, Tan J, Gloss B, *et al.* (2011): Cell type-specific channelrhodopsin-2 transgenic mice for optogenetic dissection of neural circuitry function. Nat Methods 8:745–752.
27. Bonder DE, McCarthy KD (2014): Astrocytic Gq-GPCR-linked IP3R-dependent Ca2+ signaling does not mediate neurovascular coupling in mouse visual cortex in vivo. J Neurosci 34:13139–13150.
28. Monai H, Ohkura M, Tanaka M, Oe Y, Konno A, Hirai H, *et al.* (2016): Calcium imaging reveals glial involvement in transcranial direct current stimulation-induced plasticity in mouse brain. Nat Commun 7:11100.
29. Otsu Y, Couchman K, Lyons DG, Collot M, Agarwal A, Mallet JM, *et al.* (2015): Calcium dynamics in astrocyte processes during neurovascular coupling. Nat Neurosci 18:210–218.
30. Devor A, Sakadzic S, Saisan PA, Yaseen MA, Roussakis E, Srinivasan VJ, *et al.* (2011): "Overshoot" of O(2) is required to maintain baseline tissue oxygenation at locations distal to blood vessels. J Neurosci 31:13676–13681.
31. Sakadzic S, Roussakis E, Yaseen MA, Mandeville ET, Srinivasan VJ, Arai K, *et al.* (2010): Two-photon high-resolution measurement of partial pressure of oxygen in cerebral vasculature and tissue. Nat Methods 7:755–759.
32. Lecoq J, Parpaleix A, Roussakis E, Ducros M, Goulam Houssen Y, Vinogradov SA, *et al.* (2011): Simultaneous two-photon imaging of oxygen and blood flow in deep cerebral vessels. Nat Med 17:893–898.
33. Lyons DG, Parpaleix A, Roche M, Charpak S (2016): Mapping oxygen concentration in the awake mouse brain. Elife 5.
34. Parpaleix A, Goulam Houssen Y, Charpak S (2013): Imaging local neuronal activity by monitoring PO(2) transients in capillaries. Nat Med 19:241–246.
35. Sakadzic S, Yaseen MA, Jaswal R, Roussakis E, Dale AM, Buxton RB, *et al.* (2016): Two-photon microscopy measurement of cerebral metabolic rate of oxygen using periarteriolar oxygen concentration gradients. Neurophotonics 3:045005.

36. Machler P, Wyss MT, Elsayed M, Stobart J, Gutierrez R, von Faber-Castell A, *et al.* (2016): In vivo evidence for a lactate gradient from astrocytes to neurons. Cell Metab 23:94–102.
37. Devor A, Sakadzic S, Yaseen MA, Roussakis E, Tian P, Slovin H, *et al.* (2013): Functional imaging of cerebral oxygenation with intrinsic optical contrast and phosphorescent probes. In: Weber B, Helmchen F, editors. Optical Imaging of Cortical Circuit Dynamics. New York: Springer.
38. Dunn AK, Devor A, Bolay H, Andermann ML, Moskowitz MA, Dale AM, *et al.* (2003): Simultaneous imaging of total cerebral hemoglobin concentration, oxygenation, and blood flow during functional activation. Opt Lett 28:28–30.
39. Dunn AK, Devor A, Dale AM, Boas DA (2005): Spatial extent of oxygen metabolism and hemodynamic changes during functional activation of the rat somatosensory cortex. Neuroimage 27:279–290.
40. Christie IN, Wells JA, Southern P, Marina N, Kasparov S, Gourine AV, *et al.* (2013): fMRI response to blue light delivery in the naive brain: Implications for combined optogenetic fMRI studies. Neuroimage 66:634–641.
41. Rungta RL, Osmanski BF, Boido D, Tanter M, Charpak S (2017): Light controls cerebral blood flow in naive animals. Nat Commun 8:14191.
42. Devor A, Dunn AK, Andermann ML, Ulbert I, Boas DA, Dale AM (2003): Coupling of total hemoglobin concentration, oxygenation, and neural activity in rat somatosensory cortex. Neuron 39:353–359.
43. Devor A, Ulbert I, Dunn AK, Narayanan SN, Jones SR, Andermann ML, *et al.* (2005): Coupling of the cortical hemodynamic response to cortical and thalamic neuronal activity. Proc Natl Acad Sci U S A 102:3822–3827.
44. Grinvald A, Sharon D, Omer D, Vanzetta I (2016): Imaging the neocortex functional architecture using multiple intrinsic signals: Implications for hemodynamic-based functional imaging. Cold Spring Harb Protoc 2016:pdb.top089375.
45. Jones M, Berwick J, Johnston D, Mayhew J (2001): Concurrent optical imaging spectroscopy and laser-Doppler flowmetry: The relationship between blood flow, oxygenation, and volume in rodent barrel cortex. Neuroimage 13:1002–1015.
46. Devor A, Boas D, Einevoll GT, Buxton RB, Dale AM (2012): Neuronal basis of non-invasive functional imaging: From microscopic neurovascular dynamics to BOLD fMRI. In: Choi I-Y, Gruetter R, editors. Neural Metabolism In Vivo, vol 4. New York: Springer.
47. Gorski JA, Talley T, Qiu M, Puelles L, Rubenstein JL, Jones KR (2002): Cortical excitatory neurons and glia, but not GABAergic neurons, are produced in the Emx1-expressing lineage. J Neurosci 22:6309–6314.
48. Madisen L, Mao T, Koch H, Zhuo JM, Berenyi A, Fujisawa S, *et al.* (2012): A toolbox of Cre-dependent optogenetic transgenic mice for light-induced activation and silencing. Nat Neurosci 15:793–802.
49. Ma Y, Shaik MA, Kozberg MG, Kim SH, Portes JP, Timerman D, *et al.* (2016): Resting-state hemodynamics are spatiotemporally coupled to synchronized and symmetric neural activity in excitatory neurons. Proc Natl Acad Sci U S A 113:E8463–E8471.
50. Mateo C, Knutsen PM, Tsai PS, Shih AY, Kleinfeld D (2017): Entrainment of arteriole vasomotor fluctuations by neural activity is a basis of blood-oxygenation-level-dependent "resting-state" connectivity. Neuron 96:936–948.e933.
51. Murphy MC, Chan KC, Kim SG, Vazquez AL (2018): Macroscale variation in resting-state neuronal activity and connectivity assessed by simultaneous calcium imaging, hemodynamic imaging and electrophysiology. Neuroimage 169:352–362.
52. Schwalm M, Schmid F, Wachsmuth L, Backhaus H, Kronfeld A, Aedo Jury F, *et al.* (2017): Cortex-wide BOLD fMRI activity reflects locally-recorded slow oscillation-associated calcium waves. Elife 6.
53. Albaugh DL, Salzwedel A, Van Den Berge N, Gao W, Stuber GD, Shih YY (2016): Functional magnetic resonance imaging of electrical and optogenetic deep brain stimulation at the rat nucleus accumbens. Sci Rep 6:31613.